

Phase Transformation and Switching Behavior of Magnetron Plasma Sputtered $\text{Ge}_2\text{Sb}_2\text{Se}_4\text{Te}$

Steven A. Vitale,* Paul Miller, Paul Robinson, Christopher Roberts, Vlad Liberman, Qingyang Du, Yifei Zhang, Cosmin-Constantin Popescu, Mikhail Y. Shalaginov, Myungkoo Kang, Kathleen A. Richardson, Tian Gu, Carlos Ríos, and Juejun Hu


Despite their importance in applications such as nonvolatile memory, integrated photonics, and compact optics, the crystalline-to-amorphous transition in chalcogenide phase-change materials (PCMs) is not understood. Herein, this transition in a technologically relevant infrared (IR) transparent chalcogenide material, $\text{Ge}_2\text{Sb}_2\text{Se}_4\text{Te}_1$ (GSST), is examined. Thin films of GSST using fully depleted silicon on insulator (FDSOI) microheaters are discussed and the phase transitions by polarized and unpolarized Raman spectroscopy is studied. It is confirmed that the crystalline-to-amorphous transition is driven by conversion of Ge–6Se octahedra to Ge–4Se tetrahedra with the extra Se being incorporated into an Se–Se network. This is similar to the mechanism reported in earlier work for $\text{Ge}_2\text{Sb}_2\text{Te}_5$ (GST). Recrystallization requires disrupting the Se–Se network and the crystallization activation energy is consistent with the Se–Se bond energy. Across 1000 crystallization–amorphization cycles, GSST exhibits no qualitative change in the Raman spectrum, suggesting limited film oxidation or chemical decomposition. After several hundred cycles, recrystallization is less complete, likely due to dewetting of GSST during the high-temperature amorphization step leading to compromise of the capping layer and loss of GSST. The utility of GSST as a photonic material through fabrication and testing of a GSST-coated, integrated silicon photonic Mach–Zender interferometer, is discussed.

1. Introduction

Stand-alone memory chips incorporating chalcogenide phase change materials (PCMs) such as $\text{Ge}_2\text{Sb}_2\text{Te}_5$ (GST) have been available commercially for several years. These devices exploit the resistivity difference between the amorphous and crystalline phases to encode data. Operation is robust and reliable, in part because switching the phase of a very small volume of PCM material, less than $0.001\ \mu\text{m}^3$, leads to a very large change in device resistance.^[1] Recently, researchers have explored the use of PCMs incorporated into photonic devices to create reconfigurable nonvolatile elements for applications such as optical switching,^[2] erasable photonics,^[3] tunable filters,^[4] active metasurfaces,^[5] and neuromorphic computing.^[6] PCM-enabled nonvolatile photonic devices have been demonstrated in which the PCM is deposited on one or more segments of a ring resonator,^[7] Mach–Zender interferometer,^[8] or waveguide directional coupler.^[9] A difference in optical path length is generated by setting the PCM into an amorphous (low index) or crystalline (high index) state, and light is thereby directed to one or the other output port. The state of the PCM is set using a resistive heater element: a short, high-temperature pulse amorphizes the PCM,

S. A. Vitale, P. Miller, P. Robinson, C. Roberts, V. Liberman
Advanced Materials and Microsystems Group
MIT Lincoln Laboratory
Lexington, MA 02421, USA
E-mail: steven.vitale@ll.mit.edu

Q. Du, Y. Zhang, C.-C. Popescu, M. Y. Shalaginov, T. Gu, J. Hu
Department of Materials Science & Engineering
Massachusetts Institute of Technology
Cambridge, MA 02139, USA

 The ORCID identification number(s) for the author(s) of this article can be found under <https://doi.org/10.1002/adpr.202200202>.

© 2022 The Authors. Advanced Photonics Research published by Wiley-VCH GmbH. This is an open access article under the terms of the Creative Commons Attribution License, which permits use, distribution and reproduction in any medium, provided the original work is properly cited.

DOI: 10.1002/adpr.202200202

M. Kang, K. A. Richardson
CREOL
The College of Optics & Photonics
University of Central Florida
Orlando, FL 32816, USA

C. Ríos
Department of Materials Science & Engineering
University of Maryland
College Park, MD 20724, USA

C. Ríos
Institute for Research in Electronics and Applied Physics
University of Maryland
College Park, MD 20742, USA

whereas a longer, moderate-temperature pulse recrystallizes the PCM. It is a greater challenge to use the PCM as an optical material as opposed to a resistive electrical element because in order to effect the required optical path length change one must switch a much larger volume of material (of order $1 \mu\text{m}^3$ or more) and thus new issues arise including inhomogeneous switching resulting from nonuniform heating and long thermal time constants. Further, the optical properties of the PCM must be highly reproducible upon repeated amorphization–crystallization cycles, with minimal deviation from the expected optical constants in both states. This includes stability of packaging of the component associated with their integration into/onto device platforms.

For a configurable optical computing platform, each PCM switching element must be programmed into the appropriate amorphous or crystalline state at least once, thus acting as a sort of nonvolatile read-only memory. Better would be the ability to reprogram the PCM states hundreds of times to allow for testing, debugging, and experimenting with different optical circuit configurations. $\text{Ge}_2\text{Sb}_2\text{Se}_4\text{Te}_1$ (GSST) has a low extinction coefficient in the infrared which makes it a promising PCM candidate for reconfigurable optics at telecom and mid-infrared (IR) wavelengths.^[9,10] Reducing device-to-device variability and establishing protocols (e.g., switching temperature and time) for reliable device operation is essential; doing so requires an improved understanding of the kinetics of the amorphous to crystalline transition and the mechanisms responsible for device degradation.

Several previous studies have investigated the phase change kinetics of chalcogenide PCMs, most notably GST.^[11] The present work is distinct from previous studies^[12] in that it is the first to provide a detailed study of the phase change kinetics in transparent PCMs exemplified by GSST, the first to unravel atomic structural changes during GSST phase transition, and the first to examine the physical and chemical evolution across many switching cycles.

Silicon microheaters were prepared by microfabrication on silicon-on-insulator (SOI) substrates. Highly n-doped ($\approx 10^{20} \text{cm}^{-3}$) regions were formed by phosphorous ion implantation of 220 nm-thick SOI. These $100 \mu\text{m} \times 100 \mu\text{m}$ square regions are contacted by aluminum pads forming resistive microheater elements (Figure 1). The room-temperature microheater resistance is about 60Ω . The use of doped silicon (as opposed to metal) microheaters allows fabrication of both reflective and transmissive optical devices, and also reduces insertion loss when employed in integrated photonic circuits. Small $30 \mu\text{m} \times 30 \mu\text{m}$ squares of GSST were patterned by liftoff in the center of the resistive element.

Arrays of 24 microheaters on each chip were electrically connected to a power supply and function generator to create the desired voltage waveforms. The GSST films were crystallized by applying single voltage pulses of various durations across the resistive microheater, and higher voltage pulses were used to reamorphize. As the temperature of the microheater is not measured directly during the short pulses, DC measurements were performed to characterize steady-state heater temperature as function of applied voltage. Raman spectra were recorded of the doped silicon and simultaneously of the bulk substrate silicon below the buried oxide layer. As the bulk substrate remains near room temperature but the 220 nm thick active silicon layer heats up, the 520cm^{-1} silicon Raman peak splits into two (Figure 1). The relevant temperature is determined from the red-shift of the peak corresponding to the 220 nm doped silicon layer.^[13]

The steady-state temperature measurements are then used to calibrate time-dependent COMSOL simulations of the transient temperature profile of the SOI resistive heater. The temperatures reported in this work are peak temperatures from the calibrated COMSOL simulations. Examples of two different amorphization pulses are shown in Figure S3, Supporting Information. The microheaters reach steady state in approximately $12 \mu\text{s}$.

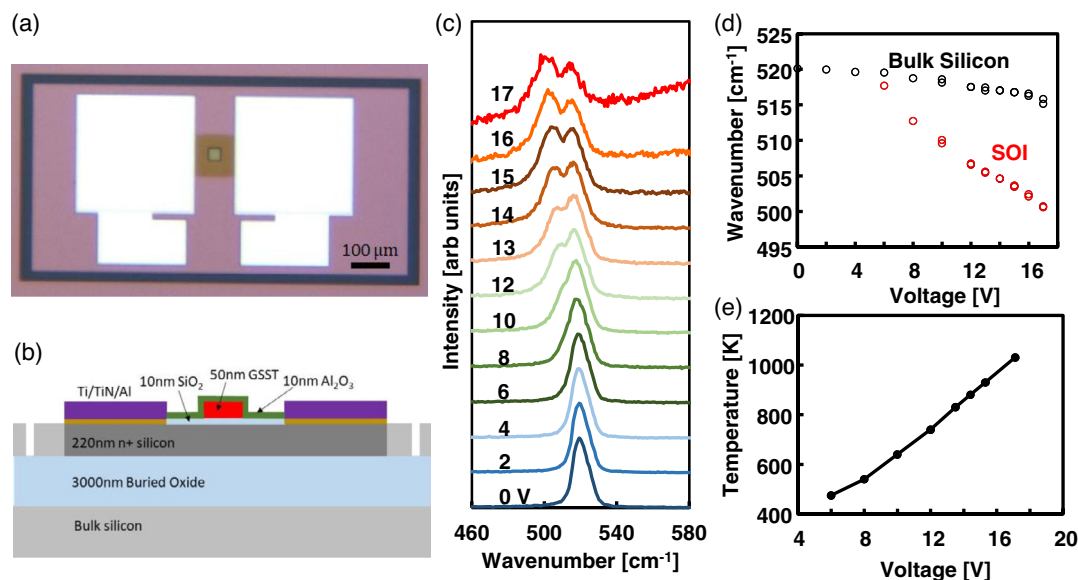


Figure 1. Microheater temperature monitoring by Raman shift. a) Photo of SOI microheater with $30 \times 30 \mu\text{m}$ GSST sample and probe pads. b) Schematic cross section of microheater. c) Raman spectrum centered on silicon line as a function of microheater voltage. d) Peak position as a function of voltage. e) SOI microheater steady-state temperature derived from peak shift.

Amorphization in less than 12 μs is possible with higher voltages as long as the amorphization temperature is achieved; Figure S3c, Supporting Information, shows the $T_{\text{am}} = 890\text{ K}$ can be attained using a 1 μs , 37.1 V pulse. This is the shortest amorphization pulse length achievable with our current devices as the pads become damaged at higher voltage. Fast quenching rates are critical to achieving the glassy state after an amorphization pulse. Figure S3b,d, Supporting Information, shows that quenching rates are typically $>10^8\text{ K s}^{-1}$ due to the small size of the microheaters and rapid thermal conduction to the silicon substrate.

2. Results and Discussion

2.1. Unpolarized Raman Spectroscopy

Figure 2a illustrates typical Raman spectra of amorphous and crystalline GSST. The spectra are raw and have not been offset or normalized. The spectrum is dominated by the broad low energy boson peak typical of glassy materials; the maximum of the boson peak in GSST is unfortunately not visible due as the spectra are truncated by the Rayleigh cutoff filter below 68 cm^{-1} . In addition, the two primary features of interest are a characteristic “crystalline” peak at 120 cm^{-1} and a characteristic “amorphous” peak at 157 cm^{-1} .^[7,14]

The Raman spectral features are broad and overlapping, so to perform a quantitative chemical analysis it is necessary to treat the boson peak and other spectral artifacts carefully. The average signal intensity is 2.8 times higher in the amorphous state than in the crystalline state, which is partially due to stronger absorption of the laser and of the scattered light by the crystalline film. Using the intensity of the 520 cm^{-1} peak from the underlying SOI in amorphous, crystalline, and no GSST present cases, along with the known GSST film thickness, the extinction coefficients (k) of GSST are calculated as 1.13 (amorphous) and 2.36 (crystalline) in the vicinity of the 633 nm excitation wavelength. Note that the difference in reflectivity of the film stack with the GSST in the crystalline versus the amorphous state was calculated to be only 2% at 633 nm, and is neglected. Using these k values, the attenuation due to absorption is calculated by

$$\frac{I}{I_0} = \frac{1}{2at}(1 - e^{-2at}) \quad (1)$$

where α is the attenuation coefficient and t is the thickness of the GSST film. To account for the natural dispersion of scattering intensity as a function of vibrational energy (Bose statistics), the reduced spectrum^[15] is calculated by

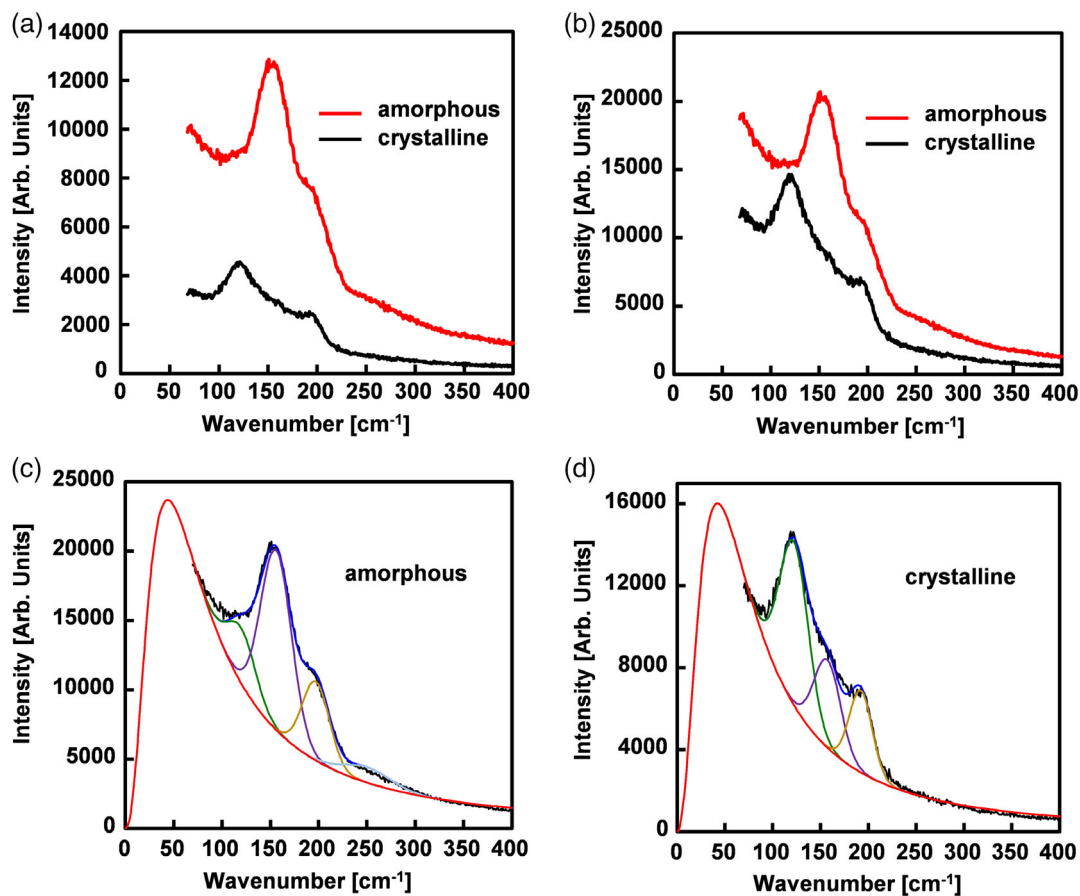


Figure 2. Raman spectra of crystalline (black) and amorphous (red) GSST. a) Raw spectra. b) Reduced Raman spectra, corrected for absorption. c) Fitting amorphous data in (b) with the boson peak, and vibrational peaks at 120, 157, 192/197, and 250 cm^{-1} . d) As in (c) for the crystalline data.

$$I^{\text{red}}(\omega) = \frac{1}{\omega(n(\omega) + 1)} \frac{1}{(\omega_0 - \omega)^4} I^{\text{exp}}(\omega) \quad (2)$$

$$n(\omega) = \frac{1}{\exp\left(\frac{\hbar\omega}{kT}\right) - 1} \quad (3)$$

where ω_0 is the excitation frequency, ω is the Raman shift, and $n(\omega)$ is the Bose–Einstein distribution. The factor $\approx \omega^4$ accounts for wavelength dependence of light scattering. The corrected reduced Raman spectra accounting for absorption are shown in Figure 2b.

To arrive at quantitative results, it is important to fit the boson peak accurately rather than simply subtract an arbitrary background signal. The exact physical phenomenon which gives rise to the boson peak is still contested,^[16] but it is associated with intermediate-range order present in glassy materials. Malinovsky and Sokolov^[17] determined that the boson peak of several amorphous materials could be fit by a universal form

$$I^{\text{Bos}}(\omega) = I_0 \frac{\omega^m}{(\omega^2 + \Omega^2)^2} \quad (4)$$

where Ω is the characteristic frequency of the intermediate-range vibrations. The authors derived $m = 2$ by assuming a form of the Raman coupling $c(\omega)$ which provided a good fit to measured spectra for the materials they investigated. The side of the boson peak visible in our spectra is also fit well by $m = 2$ for amorphous GSST. For crystalline GSST (see below), $m = 2.7$ provides a better fit so we allow m to be a variable parameter.

The boson peak area is reduced by 49% in the crystalline phase, as expected when long-range order replaces the intermediate-range order characteristic of glasses. At the same time, because there is still a significant boson peak even after GSST has been nominally completely crystallized, there still must remain significant domains of the material with structural disorder.

The vibrational spectra in both phases completely fit by four Gaussian peaks at 120, 157, 192/197, and 250 cm^{-1} , where the 192 cm^{-1} mode in crystalline GSST blueshifts slightly to 197 cm^{-1} in amorphous GSST. In a perfect crystal the Raman peaks should represent a Lorentzian lineshape, but in a glassy material disorder present along different directions and in different locations will broaden these sharp Lorentzians into Gaussian lineshapes.^[18] As the crystalline phase of GSST was equally well fit with Gaussian curves of the same full width at half maximum (FWHM), the presence of significant disorder in the crystalline phase is again supported.

To assign these vibrational peaks, Raman active modes of the GSST hexagonal crystalline structure were calculated by density functional theory (DFT). Simulated Raman spectra are shown in Figure 3, where a 10 cm^{-1} Gaussian broadening was applied to each line to match the profiles of the experimental data. The best fit results from the crystalline phase experimental data in Figure 2 are reproduced in Figure 3 where only contributions from the 120 cm^{-1} and 192 cm^{-1} peaks are included; contribution from the other two peaks associated with the amorphous phase would not be expected to appear in the simulated spectrum. The simulated spectrum also predicts two peaks, which match the experimental data very well in both relative intensity and

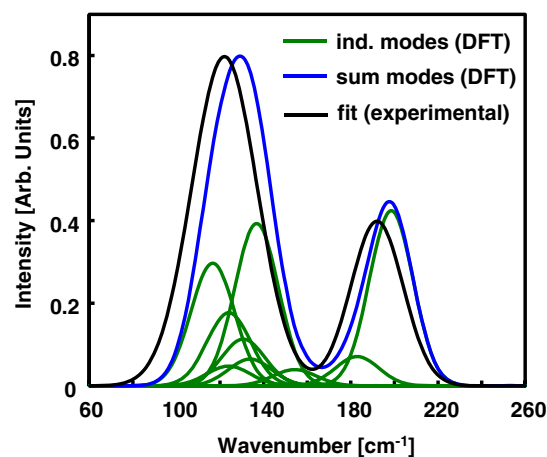


Figure 3. Individual vibrational modes calculated by DFT (gray), sum of calculated modes (blue), and fit of crystalline experimental data in Figure 2 including only 120 and 192 cm^{-1} peaks (black).

frequency. The simulations predict minimal Raman intensity at 157 cm^{-1} , indirectly confirming that measured intensity at that wavenumber in “crystalline” GSST represents residual domains of less ordered phase.

The calculated Raman modes are provided in Table 1. The modes which comprise the 120 cm^{-1} “crystalline” peak are primarily associated with motions of Se atoms in octahedral coordination with Ge. The two dominant modes comprise 1) displacement of Se atoms in the plane spanned by the a - and b -crystalline axes, and 2) vertical displacement of Se atoms along the c -axis. The dominant contribution to the 192 cm^{-1} peak (present in both the crystalline and amorphous phases) is a vertical displacement of Se atoms coordinated with Sb atoms along the c -axis.

The assignment of the characteristic crystalline peak at 120 cm^{-1} to vibrations of the Ge–6Se octahedra is consistent with prior analysis of $\text{Ge}_2\text{Se}_2\text{Te}_5$ spectra^[19] where the analogous spectral feature was assigned to Ge–6Te octahedra. We also note that the assignment of the 192 cm^{-1} feature to the Sb–6Se octahedra is supported by the fact that a Raman peak at the same location is the most prominent characteristic of the Raman spectrum of Sb_2Se_3 .^[20]

Table 1. Calculated GSST Raman active vibrational modes.

Frequency [cm^{-1}]	Raman intensity	Primary unit	Displacement axis	Degeneracy
116.6	0.35	Ge–Se octahedra	a, b	2
123.9	0.06	Sb–Se–Te octahedra	a, b	2
124.0	0.42	Ge–Se octahedra	c	1
130.6	0.27	Ge–Se octahedra	c	1
133.8	0.08	Sb–Se octahedra	a, b	2
136.8	0.46	Ge–Se octahedra	a, b	2
154.2	0.09	Ge–Se octahedra	c	1
182.9	0.17	Ge–Se octahedra	c	1
198.5	1.00	Sb–Se octahedra	c	1

It is probable that in our experimental material there are some random substitutions of Te for Se in the Ge–6Se octahedra even though these would be energetically unfavorable. By a simple reduced mass calculation, we estimate that a single Te substitution would redshift the Raman frequency by $\approx 5 \text{ cm}^{-1}$. Given the breadth of the characteristic Raman peaks, it is not possible to deconvolve such a small shift; in fact, some of the Gaussian broadening may be due to small amounts of Ge–(5Se–1Te) octahedra. We also note that the 5.9 cm^{-1} redshift in the experimental data compared to the DFT simulations (Figure 3) may be caused in part by Te substitution. As it is not possible to quantify to the extent of Te substitution however, for simplicity we will refer only to Ge–6Se octahedra.

After the transition to the amorphous phase, the 120 cm^{-1} Ge–6Se octahedral peak decreases substantially and the characteristic amorphous peak at 157 cm^{-1} appears. By analogy with previous study of $\text{Ge}_2\text{Sb}_2\text{Te}_5$,^[11g] the underlying physical transformation is likely a disruption of the Ge–6Se octahedra with most of the units changing coordination from six to four, creating Ge–4Se tetrahedra. The DFT-calculated energy per atom in Ge–4Se tetrahedra is lower than that in Ge–6Se octahedra by 8 meV. As the temperature approaches the melting point, the GSST lattice goes through random structural transformations and the lower energy tetrahedral structure increases in population even though the overall system energy increases. Upon rapid quenching, the tetrahedra remain locked in place. The 8 meV per atom then becomes a modest activation energy that must be overcome to recrystallize GSST into the globally lower energy hexagonal lattice structure.

It has been proposed^[21] that it is extremely difficult to form a glassy phase directly from octahedrally coordinated materials. Full octahedral coordination requires extensive edge and face sharing which locks the material into a rigid structure, promoting recrystallization upon quenching. In fact, we show below that GSST never forms a 100% octahedral crystal structure. There is always 10–20% tetrahedral content even in a fully crystalline film. This may help explain the excellent glass-forming ability of GSST.

The third most prominent peak, at 192 cm^{-1} in the crystalline phase, is associated with the Sb–6Se octahedra (Table 1). The peak blueshifts to 197 cm^{-1} in the amorphous phase. We believe the blueshift is due to a change in the local environment, i.e., the replacement of nearby Ge–6Se octahedral by tetrahedra, causing some distortion of the Sb–6Se octahedra. If correct, this implies that the Sb–Se sublattice of GSST remains largely unchanged during the crystalline-to-amorphous transition while the Ge–Se sublattice disorders. The constant presence of the largely ordered Sb–Se “backbone” may aid in recrystallization thus allowing for the reproducible switching observed in GSST devices.^[7]

If the crystalline-to-amorphous transition releases bonds from two Se atoms, the coordination number of those Se atoms would be reduced. To restore sixfold coordination, neighboring Se atoms may bond to each other. In fact, in the amorphous GSST Raman spectra a broad feature appears from 225 to 275 cm^{-1} , the same region as the characteristic Raman modes of amorphous selenium.^[22] That this feature is absent in crystalline GSST supports the hypothesis that Se–Se bonds form as a

result of conversion from Ge–6Se octahedra to Ge–4Se tetrahedra.

After correcting for light absorption, thermal populations, and the boson peak contribution (see Supporting Information), one can quantify the fraction of Ge–4Se and Ge–6Se units for the data in Figure 2. We calculate that crystalline GSST is composed of approximately 81% Ge–6Se units and 19% Ge–4Se units. The amorphous GSST is composed of approximately 41% Ge–6Se units and 59% Ge–4Se units. Both phases are a mixture of octahedral and tetrahedral units; it would be misleading to think of GSST as a purely binary two-state material but instead it is better characterized as a material that can be prepared along a glassy-to-crystalline continuum where increasing octahedral content locks the lattice into more long-range order.

We note that Raman mapping of the entire $30 \mu\text{m} \times 30 \mu\text{m}$ area of a well-crystallized GSST film (Figure S4, Supporting Information) reveals minimal qualitative difference in spectra from point to point, with approximately 2.7% (1σ) variation in octahedral content. Thus, the residual amorphous-like domains in the nominally crystalline state are most likely smaller than the $2 \mu\text{m}$ laser spot and are homogeneously distributed, possibly in the form of grain boundaries. It is left to future work to analyze the amorphous and crystalline domain morphology at smaller length scales by other techniques, such as transmission electron microscopy.

2.2. Polarized Raman Spectroscopy

Polarized Raman spectra can be used to confirm or reject that the spectral features in both the crystalline and amorphous phases represent the same atomic units. For example, Ge–4Se tetrahedra should show the same polarization behavior regardless if long-range order is present or not. If the spectral polarization is significantly different that would suggest that the structural units in the two phases are different, and the fact that the peak position is the same is merely coincidental.

Co- and cross-polarized (HH and HV) Raman spectra of GSST in the crystalline and amorphous phase are shown in Figure 4a,b, respectively. The depolarization ratio for each feature is provided in Table 2. The depolarization ratio for the 120 and the 157 cm^{-1} features is very similar in each phase, supporting the hypothesis that the same structures, i.e., Ge–6Se octahedra and Ge–4Se tetrahedra, are present in both phases just in different quantities.

The depolarization ratio of the boson peak is also the same in crystalline and amorphous GSST. However, it is not clear what boson peak depolarization represents as the physical vibrations giving rise to this feature are still not well understood. There have not been many reported polarization-resolved Raman studies of the boson peak, but we note that the depolarization ratio of GSST measured here is 0.41 which is comparable to the value measured in the glassy state of TeO_2 .^[21]

Circularly polarized ($\sigma^+\sigma^+$ and $\sigma^+\sigma^-$) Raman spectra of GSST in the crystalline and amorphous phase are shown in Figure 4c,d, respectively. In agreement with the linearly polarized results, the depolarization ratio of the 120 and 157 cm^{-1} peaks is the same in both phases, supporting evidence that the same structures give rise to these features in both phases.

In contrast, the circular depolarization ratio of the $192/197 \text{ cm}^{-1}$ peak is distinctly different in the crystalline and

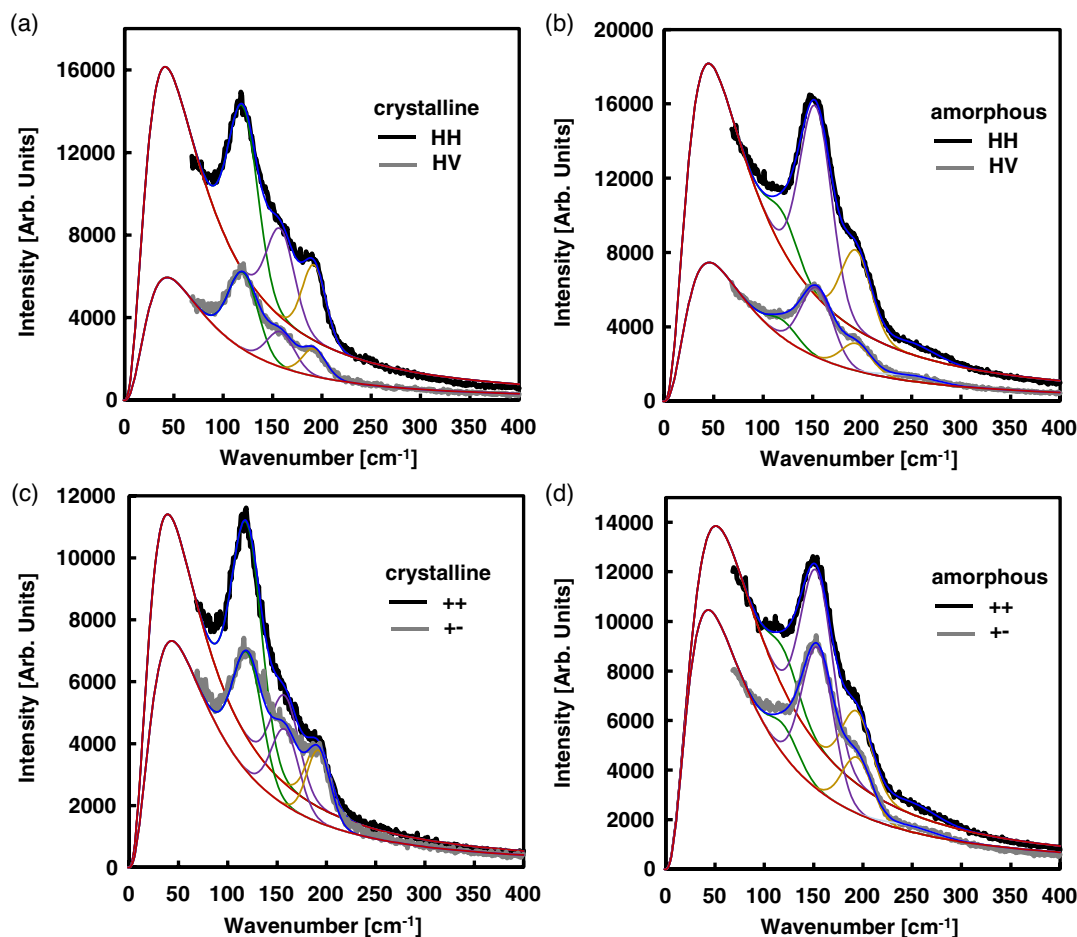


Figure 4. Polarized GSST reduced Raman spectra. Black lines are the parallel (HH) or corotating (++) data, red lines are the perpendicular (HV) or counter-rotating (+−) data. Gray lines are individual fitted peaks and the blue lines are the total fit. a) Crystalline GSST, linearly polarized; b) amorphous GSST, linearly polarized; c) crystalline GSST, circularly polarized; d) amorphous GSST, circularly polarized.

Table 2. Depolarization ratios under linear and circularly polarized excitation.

Feature	Linear		Circular	
	Crystalline	Amorphous	Crystalline	Amorphous
Boson	0.41	0.40	0.74	0.69
120 cm ^{−1} (Ge–6Se)	0.47	0.47	0.56	0.75
157 cm ^{−1} (Ge–4Se)	0.40	0.37	0.86	0.82
192/197 cm ^{−1} (Sb–6Se)	0.36	0.34	1.17	0.77
250 cm ^{−1} (Se–Se)	–	0.50	–	0.50

amorphous phases. The difference is not large given that the maximum depolarization ratio under circularly polarized excitation is 6, but given multiple measurements across different samples (not shown) the depolarization difference is statistically significant. The DFT calculations show a single Sb–6Se vibration is responsible for this mode in the crystalline state. We attribute the modest decrease in depolarization and increase in energy to an unknown deformation of the Sb–6Se octahedron in the amorphous phase; however, we cannot rule out a different structure.

Using the relative intensity of the peaks in all four polarization configurations, one can calculate the invariants of the polarizability tensor following the procedure of Nestor and Spiro.^[23] This allows a check on the internal consistency of the polarized Raman data as the asymmetric invariant γ_{as}^2 should be close to zero for Raman scattering. The results are shown in Table 3, and indeed the invariant γ_{as}^2 is close to zero. We note that it is not possible to uniquely reconstruct the complete polarizability tensor of any mode because: 1) GSST is neither isotropic nor is

Table 3. Normalized invariants of the polarizability tensor, where the first number is for the crystalline phase and the second number is for the amorphous phase.

	9/4 α^2	1/3 γ_s^2	1/3 γ_{as}^2
Boson	0.51/0.48	1.00/1.00	0.01/0.02
120 cm ^{−1}	0.36/0.47	1.00/1.00	0.00/0.07
157 cm ^{−1}	0.60/0.60	1.00/1.00	0.04/0.01
194 cm ^{−1}	0.83/0.59	1.00/1.00	0.09/0.06
250 cm ^{−1}	−/0.30	−/1.00	−/0.00

the excitation aligned with respect to the *a*- and *b*-axis, and 2) the measured peaks are convolutions of multiple modes.

2.3. Phase Transformation Kinetics

With a firmer understanding of the structure of the crystalline and amorphous phases, we now turn to the kinetics of GSST crystallization. First, we observe that as-deposited GSST is not structurally the same as GSST that has been crystallized and reamorphized. As shown in the previous section, reamorphized GSST contains a large fraction (usually 10–20%) of residual octahedral units. However, measurements of 25 as-deposited GSST samples show the octahedral fraction to be only $1.4\% \pm 0.5\%$. Qualitatively, we observe more variability in initial crystallization from as-deposited GSST compared to GSST that has been crystallized and reamorphized. Likely the higher residual octahedral content helps to initiate recrystallization. This suggests for practical purposes devices should be “set” into an initial crystalline state by annealing prior to microheater-based switching. Further data on as-deposited GSST crystallization by microheater are provided in Figure S5, Supporting Information. For comparison, across a total of 69 GSST samples crystallized by hot plate annealing the octahedral fraction is consistently $79.8\% \pm 1.2\%$.

A sparse time-temperature-transformation (TTT) diagram for GSST for microheater voltage pulse times <1 s is provided in Figure 5. The color of the symbols corresponds to the percentage of octahedral content in the material. The GSST is not constrained to two binary phases, but instead a distribution of octahedral content is observed. The dotted line in the figure outlines a nominal envelope of microheater pulse conditions which induce significant crystallization. The minimum pulse time for crystallization is ≈ 10 ms, significantly longer than the timescale for the full thickness of GSST to reach a steady-state temperature, so this 10 ms represents a minimum timescale for the Ge–4Se tetrahedral to Ge–6Se octahedral transition to take place. The minimum temperature for crystallization with subsecond pulses is 760 K. This is significantly higher than the 595 K crystallization temperature achieved with hot plate annealing. From this diagram, we calculate an approximate activation energy for crystallization of 3.2 eV. As the Ge–4Se + Se₂

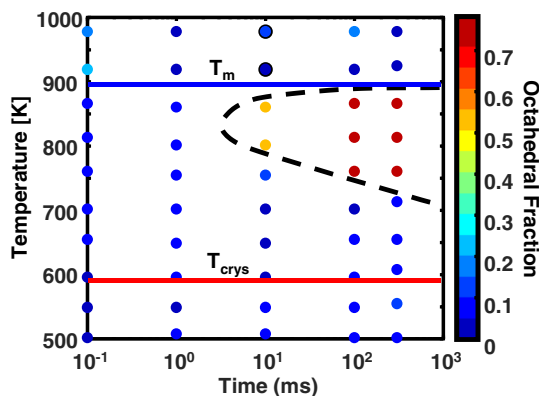


Figure 5. Fast pulse crystallization diagram of GSST. Dashed curve shows approximate envelope of crystallization conditions for subsecond pulse lengths. T_m indicates the temperature above which the GSST reamorphizes, regardless of pulse duration. T_{crys} indicates the minimum temperature for crystallization at long times (60 s).

→ Ge–6Se crystallization reaction is exothermic, one would expect the activation energy associated with the transition complex to be somewhat less than the energy required to break a Se–Se bond in the amorphous Se network formed during amorphization. The Se–Se bond dissociation energy is 3.34 eV,^[24] and thus the measured activation energy is consistent with this mechanism.

There is little room to increase the crystallization rate by increasing temperature because the GSST reamorphizes above 900 K, as shown in Figure 5. In contrast to crystallization, GSST reamorphization occurs quickly. Amorphization was consistently observed with pulse lengths from 1 μ s up to 1 ms, bounded at the lower end by the speed of the testing electronics and at the upper end by the onset of damage to the microheaters. Evidently, the amorphization kinetics associated with the octahedral to tetrahedral transition and the release of the selenium atoms are significantly faster than the recrystallization kinetics.

2.4. Switching Repeatability and Endurance

For optical applications, it is particularly important that the PCM properties are highly reproducible between switching events (see below). The octahedral content of the film was measured across many switching cycles under slightly different amorphization and crystallization conditions, as shown in Figure 6. Each panel represents a separate but nominally identical device. Panel (a) shows 20 cycles of phase switching using a long crystallization pulse of 9.5 s. Consistent switching is achieved though there is significant variation in Ge–6Se octahedral content in both the amorphous and the crystalline phases across the switching cycles. Figure 6b shows reliable switching with a shorter crystallization pulse (5 s), over more cycles and with less variability. We attribute the variability decrease to device-to-device variation, not the shorter crystallization pulse. Decreasing switching time further, Figure 6c shows similar results for 100 cycles using a 0.5 s crystallization pulse, where a very short higher temperature amorphization pulse was also employed. Consistent phase switching over 100 cycles was observed.

The switch-to-switch variability across many such tests was calculated. The average octahedral fraction in the crystalline phase is $76.4\% \pm 2.9\%$ (1σ). The average octahedral fraction in the amorphous phase is $18.9\% \pm 5.7\%$ (1σ). It is likely that much of this variation comes from our experimental technique. The microheaters are contacted using probe needles, which must support quite high currents. Variations in contact resistance will significantly affect the microheater temperature, particularly during the transient high current/high voltage amorphization steps. In Figure 6, it appears that the amorphous phase contains higher octahedral content for the first few cycles before settling in to a steady-state value, which may be related to the contacts “burning-in,” i.e., there is more voltage drop at the probe needle contacts and less across the resistive microheater for the first few cycles. This will need further investigation. As we cannot measure the microheater temperature in real time during a short voltage pulse, we cannot quantify the pulse-to-pulse temperature variation. But we suspect the variation would be significantly reduced by using wirebonded devices instead of probe needles.

To estimate the effect of octahedral/tetrahedral content on photonic circuit performance, simulations of a simple

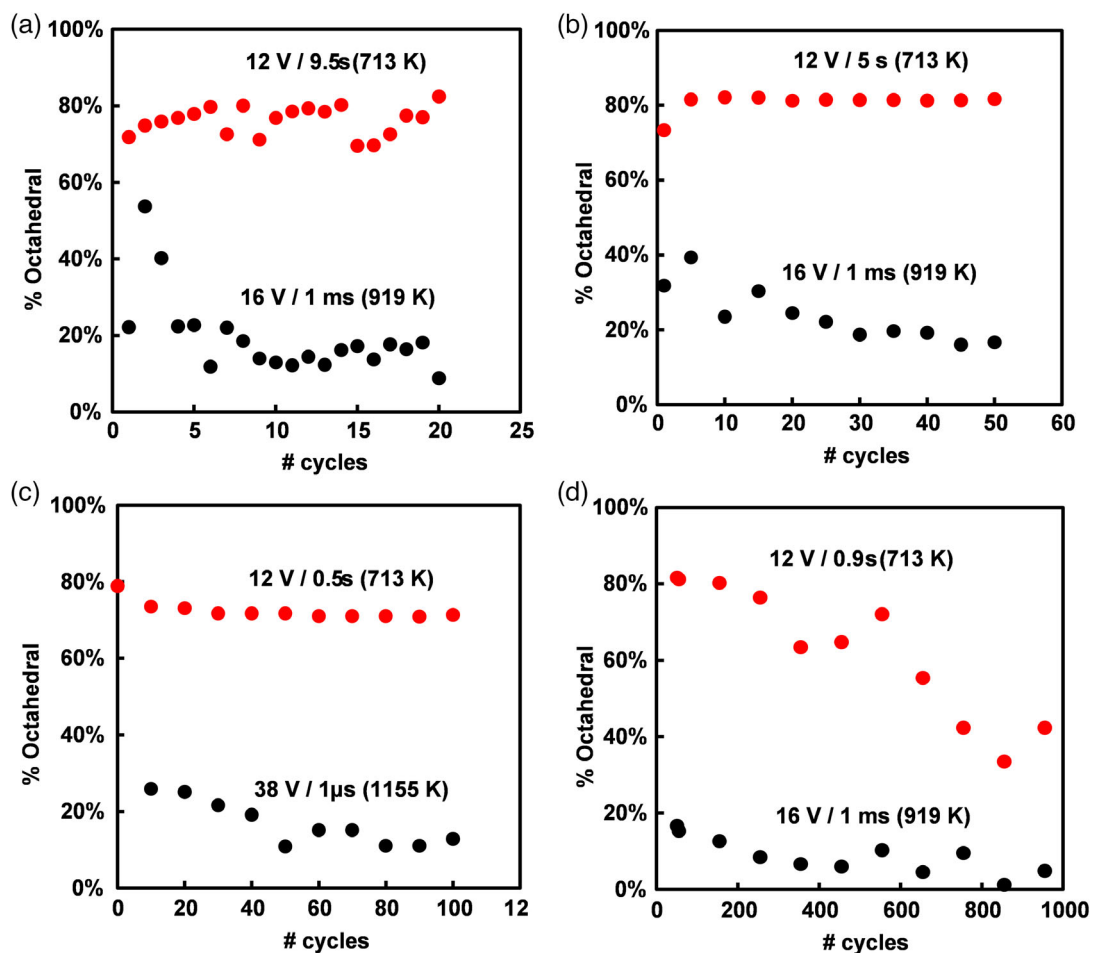


Figure 6. GSST phase switching across multiple cycles. Red dots represent Raman measurement of the Ge–6Se octahedral fraction after the recrystallization part of the cycle; black dots represent the same after the amorphization part of the cycle. The microheater pulse amplitude and duration as well as the corresponding film temperature are provided in each panel. a) Repeated crystalline-amorphous phase transitions with Raman spectra collected after each cycle; b) second device, demonstrating functionality using shorter recrystallization pulses; c) third device, demonstrating functionality using very short crystallization and amorphization pulses; d) fourth device, showing decreasing crystallinity over many cycles.

“nonperturbative” 1×2 photonic switching element were performed using the Lumerical software suite (Figure 7). The optical properties (n , k) of the GSST film were measured previously^[7] at the two amorphous and crystalline state “endpoints” and interpolated for intermediate states using the Bruggeman formula (Figure 7a). The device was designed to have maximum power to output port A when the GSST film had 23% octahedral content corresponding to the nominal “amorphous” state. The octahedral content was then varied from 23% to determine the sensitivity of the device to small variations in octahedral content from switching event to switching event. The switch insertion loss is only modestly affected by this $\pm 3\%$ octahedral content variation. The A/B output port contrast is more sensitive to octahedral content; to ensure at least 10 dB contrast between output ports the octahedral content should be controlled to within $\pm 2\%$. Though this level of control was not demonstrated in Figure 6, it is likely to be obtained with wirebonded devices as discussed above.

In addition to switch-to-switch variability, there is the issue of long-term device drift. Switching endurance over 1000 cycles is

shown in Figure 6d. The octahedral fraction in both the amorphous and crystalline decreases over many cycles. This may be more clearly seen in Figure S7, Supporting Information, which plots the data as tetrahedral fraction. Across many switching cycles, the tetrahedral content of the amorphous condition increases to nearly 100%. At the same time, the tetrahedral fraction in the crystalline condition increases linearly. This suggests that over time it becomes kinetically more difficult for the Ge–4Se tetrahedra to convert to Ge–6Se octahedra. However, even after 1000 cycles the Raman spectra is completely described by the same four peaks previously assigned; no new modes appear and no peak shifting occurs. It does not seem that the material is being “damaged” by oxidation. Instead, we suggest that over many cycles preferential loss of Se (the most volatile constituent) occurs during the high-temperature amorphization steps. Gradual loss of the amorphous Se “reservoir” in the amorphous phase would make Ge–4Se to Ge–6Se conversion both increasingly slow kinetically and stoichiometrically limited.

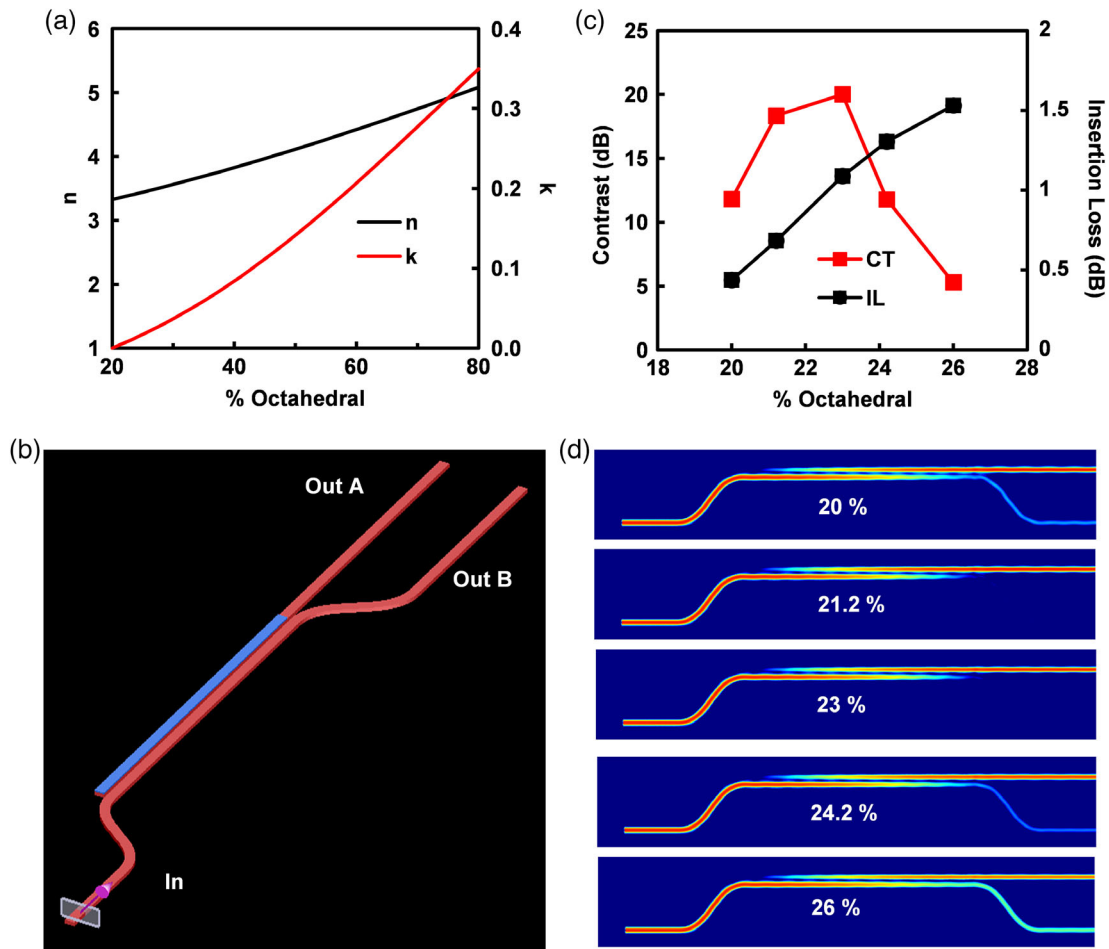


Figure 7. Simulations of optical power through 1×2 switch at $1.525 \mu\text{m}$. a) GSST optical properties as a function of GSST octahedral content, b) schematic of optical switch designed for power delivery to output A with GSST in amorphous state and output B with GSST in crystalline state (GSST patch in blue), c) optical power contrast between A and B output ports and insertion loss showing degradation in contrast as GSST octahedral content deviates from design value (23%), and d) simulated log optical power profiles for octahedral content test cases in (c).

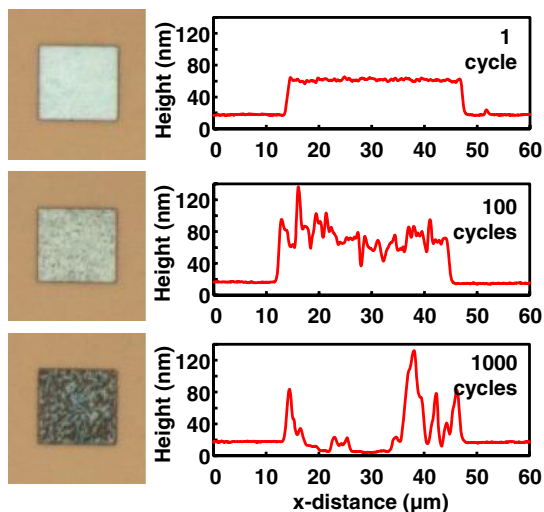


Figure 8. Photomicrographs and surface profilometry of GSST after (top) one recrystallization, (middle) 100 amorphization/recrystallization cycles, and (bottom) 1000 cycles.

Figure 8 shows optical micrographs of the $30 \times 30 \mu\text{m}$ GSST patch after one recrystallization, after 100 amorphization/recrystallization cycles, and after 1000 cycles. Dark areas which develop in the material after many cycles are determined to be thin regions by the accompanying surface profilometry measurements. Note that the surface roughness appears greatly exaggerated in Figure 8 due to the 1000-fold difference in x - and y -scales. The surface develops a wavy appearance with a spatial frequency of $1 \mu\text{m}$ or greater, and these undulations increase in height and length scale as the number of cycles increases. These morphological changes occur during the amorphization step. At the temperature required for amorphization, the GSST dewets from the underlying SiO_2 surface and begins to spheroidize to reduce surface energy (Rayleigh instability). After 100 cycles there is no apparent loss of GSST, only a wavy surface. However after 1000 cycles there is significant material loss, the mean thickness decreasing from 44.9 to 9.6 nm . We were not able to convincingly characterize whether the 10 nm -thick Al_2O_3 capping layer was still completely intact after 1000 cycles. At amorphization temperature ($>900 \text{ K}$), the Al_2O_3 layer can be pliable, permitting

deformation. For small amounts of GSST dewetting, the Al_2O_3 probably remains conformal to the GSST undulations. As GSST dewetting continues, it is possible that the Al_2O_3 layer becomes increasingly strained and eventually cracks, allowing loss of GSST through evaporation.

Though it is not yet clear how compromise of the capping layer and subsequent evaporation of GSST affect the ability to recrystallize the GSST, the two are likely related. For example, as spheroidization occurs regions of very thick and very thin GSST will develop; heat transfer to and from these regions will be somewhat different which will, in turn, affect the recrystallization in thick versus thin regions. If that is the case, then based on the data in Figure 6d compromise of the capping layer may have started to occur around 200 cycles. This is likely very dependent upon the specific device geometry and choice of amorphization conditions. Optimizing the capping layer thickness and material, as well as the amorphization process conditions, will be important to extend device endurance.

2.5. Photonic Phase Shifters

Leveraging the switching repeatability achieved with doped-silicon microheaters, we finally demonstrate nonvolatile tuning of GSST-based on-chip photonic devices. We carried out further fabrication steps (see Experimental Section) to achieve the devices shown in Figure 9a,b. Note that photonic devices were fabricated in a different facility and employed evaporated GSST, not

the magnetron sputtered GSST discussed above. We patterned microheaters with different n-doping concentrations and half-etched rib waveguides with 30 nm of GSST and 10 nm of alumina capping. In contrast to the heavily doped silicon microheaters used above for material characterization, we found moderate phosphorous doping ($\approx 4 \times 10^{18} \text{ cm}^{-3}$) in the central device area covering the waveguide offered the best trade-off between optical losses and power consumption.^[25] Moreover, 30 nm-thick GSST allows for small form-factor devices because, theoretically, the large refractive index modulation implies that a $\approx 5 \mu\text{m}$ long patch suffices to introduce a π phase shift. In Figure 9c, we demonstrate the reversible and repeatable switching between three states of a 30 nm-thick, $3 \mu\text{m}$ -long GSST cell, and the subsequent phase and amplitude modulation on a ring resonator, resulting from the changes of the real and the imaginary refractive index, respectively. After a conditioning process to establish reliable levels,^[26] we achieved over 50 cycles with no damage between three distinct positions of a single resonance peak, corresponding to the amorphous and two partially crystallized states of GSST. We used microheater pulse conditions of 20 ms at 3.5 V and $50 \mu\text{s}$ at 5 V to crystallize and amorphize, respectively. Our analysis reveals that doped-Si only contributes to $0.03 \text{ dB } \mu\text{m}^{-1}$ absorption, amorphous GSST shows zero loss, and crystalline GSST, $0.57 \text{ dB } \mu\text{m}^{-1}$. The latter is 3 times smaller than the simulated value, which suggests that not all the PCM is crystallizing and that the switching is taking place between predominantly amorphous states. In addition to the 0.06 nm (0.14π) peak shift, the modulation of the optical losses introduces the variation of

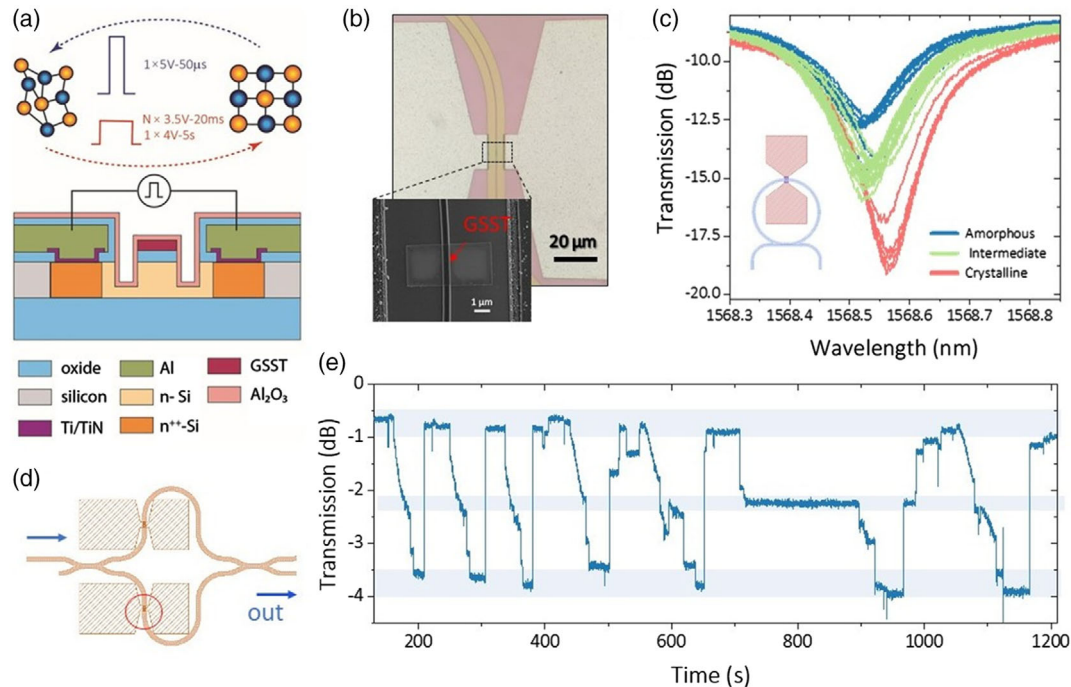


Figure 9. a) Cross-sectional sketch of photonic ridge waveguide with the experimental voltage pulses to amorphize and crystallize. The pulsed current flows from one n^{++} -doped Si contact to the other, transverse to the waveguide light propagation direction, and heats the n^- Si waveguide and the overlying patch of GSST to induce phase transformation. b) Optical and scanning electron microscopy images of a $10 \mu\text{m}$ -long microheater with $3 \mu\text{m}$ -long, 30 nm-thick GSST covering the waveguide. c) Resonance peak for three distinct GSST states on a ring with $120 \mu\text{m}$ radius, each line represents a switching event. d) Sketch of a Mach Zender interferometer switch with two 80/20-splitting directional couplers and two GSST phase shifters. e) Spectra recorded for one output channel under different GSST configurations in a $10 \mu\text{m}$ -long GSST/ $20 \mu\text{m}$ -long microheater.

the extinction ratio (ER)—upon crystallization, the device displayed higher ER but smaller Q-factor. Furthermore, we demonstrate GSST-based optical switch devices using the 2×2 Mach–Zehnder interferometer sketched in Figure 9d. We measured the variations on one output channel as a function of the state of a 10 μm -long GSST in each arm using multiple 20 ms at 3.5–4 V pulses for small quasicontinuous crystallization steps, a single 5 s at 4 V pulse for near-complete crystallization, and one or two 10–20 μs at 5 V pulses to amorphize. As shown in Figure 9e, we achieved a repeatable multilevel response upon crystallization resulting from the continuum of microstructures between approximately 20% Ge–6Se in the amorphous phase and 80% Ge–6Se in the crystalline phase, as demonstrated above.

3. Conclusions

Mechanistic understanding of the crystalline-to-amorphous transition of GSST will allow development of devices and operating procedures which minimize variability and increase device endurance. The unpolarized and polarized Raman spectroscopy measurements in the present work are consistent with a Ge–6Se octahedral to Ge–4Se tetrahedral transition, where two Se atoms are released to form an amorphous Se phase. The onset of this transition occurs very close to 900 K and at this temperature the kinetics are fairly fast, such that complete amorphization of a 50 nm-thick patch of GSST can occur in 1 μs . Recrystallization kinetics are much slower, at the onset of recrystallization near 600 K full recrystallization can take 1 min, though this can be reduced to 10–100 ms near 800 K.

Though we often refer to PCMs as being in either a ‘crystalline’ or ‘amorphous’ state, it is important to recognize that these are not binary, well-defined conditions. It would be more quantitative to characterize the state of the material by the fraction of Ge–6Se content, where 80% or greater Ge–6Se content implies a highly crystalline film and less than 20% Ge–6Se content implies a highly amorphous film. This presents both a benefit and a challenge. The benefit is that one can operate a multistate device based on different octahedral content.^[27] The challenge is to minimize the switch-to-switch variation in octahedral content to ensure consistent device operations.

In this work, we find device endurance to exceed 100 amorphization/recrystallization cycles, suggesting sufficient reliability for many commercial applications. The devices in the present work begin to degrade after 200–300 cycles, evidenced by a reduction in the amount of Ge–6Se content formed by a given recrystallization anneal pulse. We believe this is related to dewetting of the GSST during the high-temperature amorphization step which leads to crack formation in the capping layer and loss of GSST and/or Se content by evaporation. It is likely these issues can be readily addressed by engineering means however such as by a thicker capping layer, a different capping material, or changes to the time/temperature profile of the amorphization process.

4. Experimental Section

Unlike our previous work which used thermally evaporated GSST alloys,^[7,28] here the 50 nm-thick GSST film was deposited with an AJA

combinatorial magnetron sputtering system. The stoichiometry of the GSST was optimized (Figure S1, Supporting Information) through a series of experiments using Ge, Sb, Te, and GeSe₂ targets. Finally, a 10 nm Al₂O₃ capping layer was deposited by thermal atomic layer deposition.

Individual chips were mounted inside the enclosure of a Renishaw inVia Qontor Raman microscope equipped with rotatable linear polarizers and wave plates. Excitation was provided by 633 nm HeNe laser using a sample power of 2.5 mW, a 2 μm diameter spot size, and an integration time of 10 s. Tests confirmed that these conditions do not lead to inadvertent laser-induced GSST crystallization or amorphization.

Simulated Raman spectra were computed using VASP 5.6 for ionic and electronic relaxation and Raman-sc python code to extract the spectra.^[29] Projected augmented wave pseudopotentials with the Perdew–Burke–Ernzerhof version of the generalized gradient approximation (GGA) were employed.

GSST film thickness and surface roughness were measured with a Dektak XT profilometer. Optical properties of the GSST were measured before and after switching using a Filmetrics microspot NIR spectral reflectometer with a 30 μm diameter spot size.

As-deposited GSST films are amorphous, but crystallize into dendritic structures (Figure S2, Supporting Information) at temperatures near $T_{cr} = 600$ K. The crystalline phase has been shown to have a hexagonal structure;^[7] in the present work, it appears crystalline phase is oriented with the hexagonal unit cell *c*-axis perpendicular to the substrate but there is no preferred orientation of the *a*- and *b*-axes with respect to the substrate.

The photonic integrated devices were fabricated on samples containing microheaters with n^{++} regions formed with an ion-implanted dose of 10^{16} cm^{-2} and an ion energy of 80 keV, and n^+ regions with $\approx 4 \times 10^{18} \text{ cm}^{-3}$ formed with a dose of 10^{14} cm^{-2} and an ion energy of 80 keV. The contact was fabricated with a Ti/TiN barrier following a metallization with aluminum and passivation with SiO₂. The 500 nm-wide SOI waveguides and GSST cells were fabricated following two electron beam lithography steps on an Elionix ELS-F125 system. The waveguides were patterned using ZEP 520A positive photoresist followed by chlorine etching of half the silicon thickness. A liftoff process with polymethyl methacrylate (PMMA) resist was used to pattern $3 \times 4 \mu\text{m}^2$ windows for the subsequent thermal evaporation of 30 nm GSST from bulk material—synthesized using a standard melt-quench technique from high-purity (99.999%) raw elements.^[30]

Supporting Information

Supporting Information is available from the Wiley Online Library or from the author.

Acknowledgements

Approved for public release. Distribution is unlimited. This material is based upon work supported by the Under Secretary of Defense for Research and Engineering under Air Force Contract No. FA8702-15-D-0001. Any opinions, findings, conclusions, or recommendations expressed in this material are those of the author(s) and do not necessarily reflect the views of the Under Secretary of Defense for Research and Engineering.

Conflict of Interest

The authors declare no conflict of interest.

Data Availability Statement

The data that support the findings of this study are available from the corresponding author upon reasonable request.

Keywords

chalcogenide glasses, integrated photonics, metamaterials, phase change materials, Raman

Received: July 22, 2022

Revised: August 19, 2022

Published online:

- [1] a) F. Pellizzer, A. Benvenuti, B. Gleixner, Y. Kim, B. Johnson, M. Magistretti, T. Marangon, A. Pirovano, R. Bez, G. Atwood, presented at 2006 Symposium on VLSI Technology, VLSIT, Honolulu, HI, June 2006; b) D. L. Kencke, I. V. Karpov, B. G. Johnson, S. J. Lee, D. Kau, S. J. Hudgens, J. P. Reifenberg, S. D. Savransky, J. Zhang, M. D. Giles, G. Spadini, presented at 2007 IEEE Int. Electron Devices Meeting, IEDM, Washington, DC, December 2007; c) K. Baek, K. Song, S. K. Son, J. W. Oh, S.-J. Jeon, W. Kim, H. J. Kim, S. H. Oh, *NPG Asia Mater.* **2015**, *7*, 194.
- [2] a) C. Rios, M. Stegmaier, Z. Cheng, N. Youngblood, C. D. Wright, W. H. P. Pernice, H. Bhaskaran, *Opt. Mater. Express* **2018**, *8*, 2455; b) K. Kato, M. Kuwahara, H. Kawashima, T. Tsuruoka, H. Tsuda, *Appl. Phys. Express* **2017**, *10*, 072201; c) P. Xu, J. Zheng, J. K. Doyle, A. Majumdar, *ACS Photonics* **2019**, *6*, 553; d) C. Wu, H. Yu, H. Li, X. Zhang, I. Takeuchi, M. Li, *ACS Photonics* **2019**, *6*, 87; e) M. Rude, J. Pello, R. E. Simpson, J. Osmond, G. Roelkens, J. J. G. M. Van Der Tol, V. Pruneri, *Appl. Phys. Lett.* **2013**, *103*, 141119.
- [3] Y. Zhang, Q. Zhang, C. Rios, M. Y. Shalaginov, J. B. Chou, C. Roberts, P. Miller, P. Robinson, V. Liberman, M. Kang, K. A. Richardson, T. Gu, S. A. Vitale, J. Hu, *ACS Photonics* **2021**, *8*, 1903.
- [4] a) M. N. Julian, C. Williams, S. Borg, S. Bartram, H. J. Kim, *Optica* **2020**, *7*, 746; b) C. Williams, N. Hong, M. Julian, S. Borg, H. J. Kim, *Opt. Express* **2020**, *28*, 10583; c) R. Heenkenda, K. Hirakawa, A. Sarangan, *Opt. Express* **2021**, *29*, 33795.
- [5] a) J. R. Thompson, J. A. Burrow, P. J. Shah, J. Slagle, E. S. Harper, A. van Rynbach, I. Agha, M. S. Mills, *Opt. Express* **2020**, *28*, 24629; b) X. Yin, T. Steinle, L. Huang, T. Taubner, M. Wuttig, T. Zentgraf, H. Giessen, *Light: Sci. Appl.* **2017**, *6*, 17016; c) M. Y. Shalaginov, S. D. Campbell, S. An, Y. Zhang, C. Rios, E. B. Whiting, Y. Wu, L. Kang, B. Zheng, C. Fowler, H. Zhang, D. H. Werner, J. Hu, T. Gu, *Nanophotonics* **2020**, *9*, 3505; d) S. Abdollahramezani, O. Hemmatyar, M. Taghinejad, H. Taghinejad, Y. Kiarashinejad, M. Zandehshahvar, T. Fan, S. Deshmukh, A. A. Eftekhar, W. Cai, E. Pop, M. A. El-Sayed, A. Adibi, *Nano Lett.* **2021**, *21*, 1238; e) Y. Wang, P. Landreman, D. Schoen, K. Okabe, A. Marshall, U. Celano, H. S. P. Wong, J. Park, M. L. Brongersma, *Nat. Nanotechnol.* **2021**, *16*, 667; f) Q. Wang, E. T. F. Rogers, B. Gholipour, C.-M. Wang, G. Yuan, J. Teng, N. I. Zheludev, *Nat. Photonics* **2016**, *10*, 60; g) M. Y. Shalaginov, A. Sensong, Z. Yifei, Y. Fan, P. Su, V. Liberman, J. B. Chou, C. M. Roberts, K. Myungkoo, C. Rios, D. Qingyang, C. Fowler, A. Agarwal, K. A. Richardson, C. Rivero-Baleine, Z. Hualiang, H. Juejun, G. Tian, *Nat. Commun.* **2021**, *12*, 1225.
- [6] a) Y. Zhang, D. Yao, Y. Liu, C. Fang, S. Wang, G. Wang, Y. Huang, X. Yu, G. Han, Y. Hao, *IEEE Photonics J.* **2021**, *13*, 1; b) Z. Cheng, C. Rios, W. H. P. Pernice, C. David Wright, H. Bhaskaran, *Sci. Adv.* **2017**, *3*, e1700160; c) J. Feldmann, N. Youngblood, M. Karpov, H. Gehring, X. Li, M. Stappers, M. Gallo, X. Fu, A. Lukashchuk, A. S. Raja, J. Liu, C. D. Wright, A. Sebastian, T. J. Kippenberg, W. H. P. Pernice, H. Bhaskaran, *Nature* **2021**, *589*, 52; d) C. Wu, H. Yu, S. Lee, R. Peng, I. Takeuchi, M. Li, *Nat. Commun.* **2021**, *12*, 96; e) S. Abdollahramezani, O. Hemmatyar, H. Taghinejad, A. Krasnok, Y. Kiarashinejad, M. Zandehshahvar, A. Alu, A. Adibi, *arXiv*, **2020**.
- [7] Z. Yifei, J. B. Chou, L. Junying, L. Huashan, D. Qingyang, A. Yadav, Z. Si, M. Y. Shalaginov, F. Zhuoran, Z. Huikai, C. Roberts, P. Robinson, B. Bohlin, C. Rios, L. Hongtao, K. Myungkoo, G. Tian, J. Warner, V. Liberman, K. Richardson, H. Juejun, *Nat. Commun.* **2019**, *10*, 4279.
- [8] M. Delaney, I. Zeimpekis, H. Du, X. Yan, M. Banakar, D. J. Thomson, D. W. Hewak, O. L. Muskens, *Sci. Adv.* **2021**, *7*, eabg3500.
- [9] Q. Zhang, Y. Zhang, L. I. Junying, R. Soref, T. Gu, J. Hu, *Opt. Lett.* **2018**, *43*, 94.
- [10] D. Sahoo, R. Naik, *Mater. Res. Bull.* **2022**, *148*, 111679.
- [11] a) J. L. F. Da Silva, A. Walsh, W. Su-Huai, H. Lee, *J. Appl. Phys.* **2009**, *106*, 113509; b) R. De Bastiani, E. Carria, S. Gibilisco, A. Mio, C. Bongiorno, F. Piccinelli, M. Bettinelli, A. R. Pennisi, M. G. Grimaldi, E. Rimini, *J. Appl. Phys.* **2010**, *107*, 113521; c) R. Golovchak, Y. G. Choi, S. Kozyukhin, Y. Chigirinsky, A. Kovalskiy, P. Xiong-Skiba, J. Trimble, R. Pafchek, H. Jain, *Appl. Surf. Sci.* **2015**, *332*, 533; d) K. S. Andrikopoulos, S. N. Yannopoulos, A. V. Kolobov, P. Fons, J. Tominaga, *J. Phys. Chem. Solids* **2007**, *68*, 1074; e) J. Pries, S. Wei, M. Wuttig, P. Lucas, *Adv. Mater.* **2019**, *31*, 1900784; f) S. Guo, Z. Hu, X. Ji, T. Huang, X. Zhang, L. Wu, Z. Song, J. Chu, *RSC Adv.* **2014**, *4*, 57218; g) A. V. Kolobov, P. Fons, A. I. Frenkel, A. L. Ankudinov, J. Tominaga, T. Uruga, *Nat. Mater.* **2004**, *3*, 703.
- [12] S. X. Gan, C. K. Lai, W. Y. Chong, D. Y. Choi, S. Madden, H. Ahmad, *Opt. Mater.* **2021**, *120*, 111450.
- [13] T. R. Hart, R. L. Aggarwal, B. Lax, *Phys. Rev. B* **1970**, *1*, 638.
- [14] C. Ríos, Y. Zhang, M. Y. Shalaginov, S. Deckoff-Jones, H. Wang, S. An, H. Zhang, M. Kang, K. A. Richardson, C. Roberts, J. B. Chou, V. Liberman, S. A. Vitale, J. Kong, T. Gu, J. Hu, *Adv. Photonics Res.* **2021**, *2*, 2000034.
- [15] M. H. Brooker, O. F. Nielsen, E. Praestgaard, *J. Raman Spectrosc.* **1988**, *19*, 71.
- [16] J. Schroeder, W. Weimin, J. L. Apkarian, M. Lee, H. Luu-Gen, C. T. Moynihan, presented at *Sixteenth University Conf. on Glass Science*, Netherlands, August 2003.
- [17] V. K. Malinovsky, A. P. Sokolov, *Solid State Commun.* **1986**, *57*, 757.
- [18] Y. Guo, Ph.D. University of Central Florida, Orlando, FL, **2006**.
- [19] G. C. Sosso, S. Caravati, R. Mazzarello, M. Bernasconi, *Phys. Rev. B Condens. Matter Mater. Phys.* **2011**, *83*, 134201.
- [20] A. Shongalova, M. R. Correia, B. Vermang, J. M. V. Cunha, P. M. P. Salome, P. A. Fernandes, *MRS Commun.* **2018**, *8*, 865.
- [21] A. G. Kalampounias, G. Tsilomelekis, S. Boghosian, *J. Chem. Phys.* **2015**, *142*, 154503.
- [22] V. V. Poborchii, A. V. Kolobov, K. Tanaka, *Appl. Phys. Lett.* **1998**, *72*, 1167.
- [23] J. Nestor, T. G. Spiro, *J. Raman Spectrosc.* **1973**, *1*, 539.
- [24] *CRC Handbook of Chemistry and Physics* (Ed: R. C. Weast), CRC Press, Cleveland **1976**.
- [25] C. Ríos, Q. Du, Y. Zhang, C.-C. Popescu, M. Y. Shalaginov, P. Miller, C. Roberts, M. Kang, K. A. Richardson, T. Gu, S. A. Vitale, J. Hu, **2021**, <https://doi.org/10.48550/ARXIV.2105.06010>.
- [26] C. Rios, M. Stegmaier, P. Hosseini, D. Wang, T. Scherer, C. D. Wright, H. Bhaskaran, W. H. P. Pernice, *Nat. Photonics* **2015**, *9*, 725.
- [27] C. Rios, Q. Du, Y. Zhang, M. Shalaginov, P. Miller, P. Robinson, C. Roberts, M. Kang, K. A. Richardson, T. Gu, S. Vitale, J. Hu, presented at *2021 Conf. on Lasers and Electro-Optics, CLEO 2021*, Virtual, Online, USA, May 2021.

- [28] Y. Zhang, C. Fowler, J. Liang, B. Azhar, M. Y. Shalaginov, S. Deckoff-Jones, S. An, J. B. Chou, C. M. Roberts, V. Liberman, M. Kang, C. Rios, K. A. Richardson, C. Rivero-Baleine, T. Gu, H. Zhang, J. Hu, *Nat. Nanotechnol.* **2021**, *16*, 661.
- [29] D. Porezag, M. R. Pederson, *Phys. Rev. B Condens. Matter* **1996**, *54*, 7830.
- [30] L. Petit, N. Carlie, H. Chen, S. Gaylord, J. Massera, G. Boudebs, J. Hu, A. Agarwal, L. Kimerling, K. Richardson, *J. Solid State Chem.* **2009**, *182*, 2756.